

Visualization of phase retardation of deep posterior eye by polarization-sensitive swept-source optical coherence tomography with 1- μm probe

Masahiro Yamanari, Yiheng Lim, Shuichi Makita, and Yoshiaki Yasuno

Computational Optics Group in the University of Tsukuba, Tsukuba, Ibaraki, Japan
yamanari@optlab2.bk.tsukuba.ac.jp

<http://optics.bk.tsukuba.ac.jp/COG/>

Abstract: Polarization-sensitive optical coherence tomography (PS-OCT) can measure cross-sectional and volumetric images of birefringence in fibrous tissues that provides additional contrast to the intensity images. In this study, we develop polarization-sensitive swept-source OCT (PS-SS-OCT) at 1 μm for deep penetration of the sclera and lamina cribrosa in the posterior part of human eyes. A calibration method for polarization mode dispersion of a circulator, which is employed to conserve the optical power of the interferometer and achieve system sensitivity sufficient for retinal imaging is demonstrated. The A-scan rate, the axial resolution, and the sensitivity of the PS-SS-OCT are 28,000 Hz, 11.0 μm , 94.2 dB, respectively. The posterior part of the eyes of a healthy male subject are measured *in vivo*. Phase-retardation images show birefringence of deep sclera and lamina cribrosa and enhance the contrast which is not visible in the intensity images. In addition, unlike conventional OCT, our PS-SS-OCT showed polarization-insensitive intensity images, in which an artifact created by the birefringence of sclera has been successfully eliminated.

© 2009 Optical Society of America

OCIS codes: (170.4500) Optical coherence tomography; (170.3880) Medical and biological imaging; (170.4460) Ophthalmic optics and devices; (260.5430) Polarization; (260.1440) Birefringence; (110.4500) Optical coherence tomography.

References and links

1. D. Huang, E. Swanson, C. Lin, J. Schuman, W. Stinson, W. Chang, M. Hee, T. Flotte, K. Gregory, C. Puliafito, and J. Fujimoto, "Optical coherence tomography," *Science* **254**, 1178–1181 (1991).
2. M. R. Hee, D. Huang, E. A. Swanson, and J. G. Fujimoto, "Polarization-sensitive low-coherence reflectometer for birefringence characterization and ranging," *J. Opt. Soc. Am. B* **9**, 903–908 (1992).
3. J. F. de Boer, T. E. Milner, M. J. C. van Gemert, and J. S. Nelson, "Two-dimensional birefringence imaging in biological tissue by polarization-sensitive optical coherence tomography," *Opt. Lett.* **22**, 934–936 (1997).
4. B. Cense, T. C. Chen, B. H. Park, M. C. Pierce, and J. F. de Boer, "In vivo depth-resolved birefringence measurements of the human retinal nerve fiber layer by polarization-sensitive optical coherence tomography," *Opt. Lett.* **27**, 1610–1612 (2002).

5. B. Cense, T. C. Chen, B. H. Park, M. C. Pierce, and J. F. de Boer, "Thickness and Birefringence of Healthy Retinal Nerve Fiber Layer Tissue Measured with Polarization-Sensitive Optical Coherence Tomography," *Invest. Ophthalmol. Vis. Sci.* **45**, 2606–2612 (2004).
6. M. Mujat, B. H. Park, B. Cense, T. C. Chen, and J. F. de Boer, "Autocalibration of spectral-domain optical coherence tomography spectrometers for in vivo quantitative retinal nerve fiber layer birefringence determination," *J. Biomed. Opt.* **12**, 041205 (2007).
7. M. Yamanari, M. Miura, S. Makita, T. Yatagai, and Y. Yasuno, "Phase retardation measurement of retinal nerve fiber layer by polarization-sensitive spectral-domain optical coherence tomography and scanning laser polarimetry," *J. Biomed. Opt.* **13**, 014013 (2008).
8. E. Götzinger, M. Pircher, and C. K. Hitzenberger, "High speed spectral domain polarization sensitive optical coherence tomography of the human retina," *Opt. Express* **13**, 10217–10229 (2005). URL <http://www.opticsexpress.org/abstract.cfm?URI=oe-13-25-10217>.
9. E. Götzinger, M. Pircher, B. Baumann, C. Hirn, C. Vass, and C. K. Hitzenberger, "Analysis of the origin of atypical scanning laser polarimetry patterns by polarization-sensitive optical coherence tomography," *Invest. Ophthalmol. Vis. Sci.* **49**, 5366–5372 (2008).
10. B. Cense, "Optical coherence tomography for retinal imaging," Ph.D. thesis, University of Twente (2005).
11. B. Cense, M. Mujat, T. C. Chen, B. H. Park, and J. F. de Boer, "Polarization-sensitive spectral-domain optical coherence tomography using a single line scan camera," *Opt. Express* **15**, 2421–2431 (2007). URL <http://www.opticsexpress.org/abstract.cfm?URI=oe-15-5-2421>.
12. M. Miura, M. Yamanari, T. Iwasaki, A. E. Elsner, S. Makita, T. Yatagai, and Y. Yasuno, "Imaging polarimetry in age-related macular degeneration," *Invest. Ophthalmol. Vis. Sci.* **49**, 2661–2667 (2008).
13. E. Götzinger, M. Pircher, B. Baumann, C. Ahlers, W. Geitzenauer, U. Schmidt-Erfurth, and C. K. Hitzenberger, "Three-dimensional polarization sensitive OCT imaging and interactive display of the human retina," *Opt. Express* **17**, 4151–4165 (2009). URL <http://www.opticsexpress.org/abstract.cfm?URI=oe-17-5-4151>.
14. M. Yamanari, S. Makita, and Y. Yasuno, "Polarization-sensitive swept-source optical coherence tomography with continuous source polarization modulation," *Opt. Express* **16**, 5892–5906 (2008). URL <http://www.opticsexpress.org/abstract.cfm?URI=oe-16-8-5892>.
15. M. Zhao and J. A. Izatt, "Single-camera sequential-scan-based polarization-sensitive SDOCT for retinal imaging," *Opt. Lett.* **34**, 205–207 (2009).
16. Y. Yasuno, M. Yamanari, K. Kawana, T. Oshika, and M. Miura, "Investigation of post-glaucoma-surgery structures by three-dimensional and polarization sensitive anterior eye segment optical coherence tomography," *Opt. Express* **17**, 3980–3996 (2009). URL <http://www.opticsexpress.org/abstract.cfm?URI=oe-17-5-3980>.
17. M. Pircher, E. Götzinger, R. Leitgeb, H. Sattmann, O. Findl, and C. Hitzenberger, "Imaging of polarization properties of human retina in vivo with phase resolved transversal PS-OCT," *Opt. Express* **12**, 5940–5951 (2004). URL <http://www.opticsexpress.org/abstract.cfm?URI=oe-12-24-5940>.
18. M. Pircher, E. Götzinger, O. Findl, S. Michels, W. Geitzenauer, C. Leydolt, U. Schmidt-Erfurth, and C. K. Hitzenberger, "Human Macula Investigated In Vivo with Polarization-Sensitive Optical Coherence Tomography," *Invest. Ophthalmol. Vis. Sci.* **47**, 5487–5494 (2006).
19. E. Götzinger, M. Pircher, W. Geitzenauer, C. Ahlers, B. Baumann, S. Michels, U. Schmidt-Erfurth, and C. K. Hitzenberger, "Retinal pigment epithelium segmentation by polarization sensitive optical coherence tomography," *Opt. Express* **16**, 16416–16428 (2008). URL <http://www.opticsexpress.org/abstract.cfm?URI=oe-16-21-16410>.
20. R. Leitgeb, C. Hitzenberger, and A. Fercher, "Performance of fourier domain vs. time domain optical coherence tomography," *Opt. Express* **11**, 889–894 (2003). URL <http://www.opticsexpress.org/abstract.cfm?URI=oe-11-8-889>.
21. J. F. de Boer, B. Cense, B. H. Park, M. C. Pierce, G. J. Tearney, and B. E. Bouma, "Improved signal-to-noise ratio in spectral-domain compared with time-domain optical coherence tomography," *Opt. Lett.* **28**, 2067–2069 (2003). URL <http://ol.osa.org/abstract.cfm?URI=ol-28-21-2067>.
22. M. Wojtkowski, R. Leitgeb, A. Kowalczyk, T. Bajraszewski, and A. F. Fercher, "In vivo human retinal imaging by Fourier domain optical coherence tomography," *J. Biomed. Opt.* **7**, 457–463 (2002).
23. N. Nassif, B. Cense, B. H. Park, S. H. Yun, T. C. Chen, B. E. Bouma, G. J. Tearney, and J. F. de Boer, "In vivo human retinal imaging by ultrahigh-speed spectral domain optical coherence tomography," *Opt. Lett.* **29**, 480–482 (2004).
24. Y. Yasuno, S. Makita, Y. Sutoh, M. Itoh, and T. Yatagai, "Birefringence imaging of human skin by polarization-sensitive spectral interferometric optical coherence tomography," *Opt. Lett.* **27**, 1803–1805 (2002).
25. Y. Yasuno, S. Makita, T. Endo, M. Itoh, T. Yatagai, M. Takahashi, C. Katada, and M. Mutoh, "Polarization-sensitive complex Fourier domain optical coherence tomography for Jones matrix imaging of biological samples," *Appl. Phys. Lett.* **85**, 3023–3025 (2004).
26. B. Povazay, K. Bizheva, B. Hermann, A. Unterhuber, H. Sattmann, A. Fercher, W. Drexler, C. Schubert, P. Ahnelt, M. Meier, R. Holzwarth, W. Wadsworth, J. Knight, and P. S. J. Russell, "Enhanced visualization of choroidal vessels using ultrahigh resolution ophthalmic OCT at 1050 nm," *Opt. Express* **11**, 1980–1986 (2003). URL <http://www.opticsexpress.org/abstract.cfm?URI=oe-11-17-1980>.
27. A. Unterhuber, B. Povazay, B. Hermann, H. Sattmann, A. Chavez-Pirson, and W. Drexler, "In vivo retinal optical

- coherence tomography at 1040 nm - enhanced penetration into the choroid," *Opt. Express* **13**, 3252–3258 (2005). URL <http://www.opticsexpress.org/abstract.cfm?URI=oe-13-9-3252>.
28. B. Povazay, B. Hermann, A. Unterhuber, B. Hofer, H. Sattmann, F. Zeiler, J. E. Morgan, C. Falkner-Radler, C. Glittenberg, S. Blinder, and W. Drexler, "Three-dimensional optical coherence tomography at 1050 nm versus 800 nm in retinal pathologies: enhanced performance and choroidal penetration in cataract patients," *J. Biomed. Opt.* **12**, 041211 (2007).
 29. S. Makita, T. Fabritius, and Y. Yasuno, "Full-range, high-speed, high-resolution 1 μ m spectral-domain optical coherence tomography using BM-scan for volumetric imaging of the human posterior eye," *Opt. Express* **16**, 8406–8420 (2008). URL <http://www.opticsexpress.org/abstract.cfm?URI=oe-16-12-8406>.
 30. P. Puvanathan, P. Forbes, Z. Ren, D. Malchow, S. Boyd, and K. Bizheva, "High-speed, high-resolution Fourier-domain optical coherence tomography system for retinal imaging in the 1060 nm wavelength region," *Opt. Lett.* **33**, 2479–2481 (2008). URL <http://ol.osa.org/abstract.cfm?URI=ol-33-21-2479>.
 31. B. Povazay, B. Hermann, B. Hofer, V. Kajic, E. Simpson, T. Bridgford, and W. Drexler, "Wide-field optical coherence tomography of the choroid in vivo," *Invest. Ophthalmol. Vis. Sci.* **50**, 1856–1863 (2009).
 32. B. Povazay, B. Hofer, C. Torti, B. Hermann, A. R. Tumlinson, M. Esmaelpour, C. A. Egan, A. C. Bird, and W. Drexler, "Impact of enhanced resolution, speed and penetration on three-dimensional retinal optical coherence tomography," *Opt. Express* **17**, 4134–4150 (2009). URL <http://www.opticsexpress.org/abstract.cfm?URI=oe-17-5-4134>.
 33. E. C. Lee, J. F. de Boer, M. Mujat, H. Lim, and S. H. Yun, "In vivo optical frequency domain imaging of human retina and choroid," *Opt. Express* **14**, 4403–4411 (2006). URL <http://www.opticsexpress.org/abstract.cfm?URI=oe-14-10-4403>.
 34. Y. Yasuno, Y. Hong, S. Makita, M. Yamanari, M. Akiba, M. Miura, and T. Yatagai, "In vivo high-contrast imaging of deep posterior eye by 1- μ m swept source optical coherence tomography and scattering optical coherence angiography," *Opt. Express* **15**, 6121–6139 (2007). URL <http://www.opticsexpress.org/abstract.cfm?URI=oe-15-10-6121>.
 35. R. Huber, D. C. Adler, V. J. Srinivasan, and J. G. Fujimoto, "Fourier domain mode locking at 1050 nm for ultra-high-speed optical coherence tomography of the human retina at 236,000 axial scans per second," *Opt. Lett.* **32**, 2049–2051 (2007). URL <http://ol.osa.org/abstract.cfm?URI=ol-32-14-2049>.
 36. V. J. Srinivasan, D. C. Adler, Y. Chen, I. Gorczynska, R. Huber, J. S. Duker, J. S. Schuman, and J. G. Fujimoto, "Ultrahigh-speed optical coherence tomography for three-dimensional and en face imaging of the retina and optic nerve head," *Invest. Ophthalmol. Vis. Sci.* **49**, 5103–5110 (2008).
 37. M. Choma, M. Sarunic, C. Yang, and J. Izatt, "Sensitivity advantage of swept source and Fourier domain optical coherence tomography," *Opt. Express* **11**, 2183–2189 (2003). URL <http://www.opticsexpress.org/abstract.cfm?URI=oe-11-18-2183>.
 38. S. Yun, G. Tearney, J. de Boer, N. Iftimia, and B. Bouma, "High-speed optical frequency-domain imaging," *Opt. Express* **11**, 2953–2963 (2003). URL <http://www.opticsexpress.org/abstract.cfm?URI=oe-11-22-2953>.
 39. B. Vakoc, S. Yun, J. de Boer, G. Tearney, and B. Bouma, "Phase-resolved optical frequency domain imaging," *Opt. Express* **13**, 5483–5493 (2005). URL <http://www.opticsexpress.org/abstract.cfm?URI=oe-13-14-5483>.
 40. American National Standards Institute, *American national standard for safe use of lasers z136.1* (Laser Institute of America, Orlando, FL, 2000).
 41. B. H. Park, M. C. Pierce, B. Cense, and J. F. de Boer, "Jones matrix analysis for a polarization-sensitive optical coherence tomography system using fiber-optic components," *Opt. Lett.* **29**, 2512–2514 (2004).
 42. R. R. Allingham, K. F. Damji, S. Freedman, S. E. Moroi, and G. Shafranov, eds., *Shields' Textbook of Glaucoma*, 5th ed. (Lippincott Williams & Wilkins, 2005).
 43. J. F. de Boer and T. E. Milner, "Review of polarization sensitive optical coherence tomography and Stokes vector determination," *Journal of Biomedical Optics* **7**, 359–371 (2002).
 44. X.-R. Huang, H. Bagga, D. S. Greenfield, and R. W. Knighton, "Variation of Peripapillary Retinal Nerve Fiber Layer Birefringence in Normal Human Subjects," *Invest. Ophthalmol. Vis. Sci.* **45**, 3073–3080 (2004).
 45. M. J. Hogan, J. A. Alvarado, and J. E. Weddell, *Histology of the human eye: an atlas and textbook* (Saunders, 1971).
 46. Y. Chen, D. M. de Bruin, C. Kerbage, and J. F. de Boer, "Spectrally balanced detection for optical frequency domain imaging," *Opt. Express* **15**, 16390–16399 (2007). URL <http://www.opticsexpress.org/abstract.cfm?URI=oe-15-25-16390>.
 47. A. M. Rollins and J. A. Izatt, "Optimal interferometer designs for optical coherence tomography," *Opt. Lett.* **24**, 1484–1486 (1999).
 48. S. Jiao, M. Todorovic, G. Stoica, and L. V. Wang, "Fiber-based polarization-sensitive Mueller matrix optical coherence tomography with continuous source polarization modulation," *Appl. Opt.* **44**, 5463–5467 (2005).
 49. M. Yamanari, S. Makita, V. D. Madjarova, T. Yatagai, and Y. Yasuno, "Fiber-based polarization-sensitive Fourier domain optical coherence tomography using B-scan-oriented polarization modulation method," *Opt. Express* **14**, 6502–6515 (2006). URL <http://www.opticsexpress.org/abstract.cfm?URI=oe-14-14-6502>.
 50. C. E. Saxer, J. F. de Boer, B. H. Park, Y. Zhao, Z. Chen, and J. S. Nelson, "High-speed fiber based polarization-sensitive optical coherence tomography of in vivo human skin," *Opt. Lett.* **25**, 1355–1357 (2000).

51. W. Oh, S. Yun, B. Vakoc, M. Shishkov, A. Desjardins, B. Park, J. de Boer, G. Tearney, and B. Bouma, "High-speed polarization sensitive optical frequency domain imaging with frequency multiplexing," *Opt. Express* **16**, 1096–1103 (2008). URL <http://www.opticsexpress.org/abstract.cfm?URI=oe-16-2-1096>.
-

1. Introduction

Optical coherence tomography (OCT) is an imaging technique, which can be used to obtain cross-sectional images of highly scattering biological samples using low-coherence interferometry [1]. Polarization-sensitive OCT (PS-OCT) is a functional extension of OCT, which can measure the birefringence of the samples [2, 3]. PS-OCT has been employed in ophthalmic imaging to measure the birefringence of fibrous tissues [4–16]. Quantitative *in vivo* measurements of the thickness and birefringence of retinal nerve fiber layer (RNFL) using PS-OCT have been demonstrated [4–7]. The birefringence of the sclera around the optic nerve head (ONH) and lamina cribrosa in the ONH which consist of collagen fibers was visualized using PS-OCT [7–9]. Polarization scrambling at retinal pigment epithelium (RPE) has been observed [8, 12, 17, 18], and the segmentation method of RPE was developed using PS-OCT [15, 19]. Other studies have demonstrated that characteristic birefringence in patients with age-related macular degeneration could be used to enhance the contrast of the fibrosis in their retinal images [12, 13]. The above studies indicate that retinal PS-OCT would be useful in examining damaged fibrous tissues and abnormal fibrosis in diseased eyes.

In the early development of PS-OCT, the time domain technique was used [2–4]. Spectral domain OCT (SD-OCT) is the second-generation technology of OCT, which exhibits higher sensitivity than the time domain OCT [20, 21]. High-speed SD-OCT for retinal imaging was developed owing to its advantageous high sensitivity [22, 23]. Polarization sensitivity was applied to SD-OCT and the imaging of nonophthalmic samples was reported [24, 25]. Recently, retinal imaging by polarization-sensitive SD-OCT (PS-SD-OCT) has been demonstrated using several algorithms [6–8, 10, 11, 15, 19].

Until now, retinal imaging by PS-OCT has been carried out using the 800 nm wavelength band, which is the standard wavelength for retinal OCT imaging. The penetration of retinal OCT at 800 nm is limited due to the absorption and scattering of RPE. One of the approaches to overcome this penetration limitation is the use of an alternative probing wavelength of 1 μm . It was found that the use of the wavelength band of 1 μm enabled a relatively deep penetration of the choroid through the RPE [26, 27]. High-speed OCT at 1 μm wavelength has been demonstrated using SD-OCT [28–32]. It also has been demonstrated using swept-source OCT (SS-OCT) [33–36], which has the advantage of high sensitivity as well as SD-OCT [37, 38]. It is reasonable to expect that PS-OCT performed at 1 μm wavelength can reveal more interesting properties of the deep posterior part of the eye. However, retinal imaging by PS-OCT at 1 μm wavelength using any type of OCT techniques has not been demonstrated thus far.

In this paper, we describe a PS-SS-OCT system at 1 μm wavelength and demonstrate phase-retardation imaging of the deep posterior part of the eye using this system. Using a method for continuous source polarization modulation [14], we obtain depth-resolved full Jones matrices of the sample with a single depth scan. The power-conserving interferometer is constructed using a circulator, whose polarization mode dispersion was calibrated in the system. We demonstrate that the use of a 1 μm probe for retinal PS-OCT is suitable to visualize the birefringence of the sclera and the lamina cribrosa in their phase-retardation images.

2. System

2.1. System configuration

The PS-SS-OCT system for imaging at 1 μm was constructed using a fiber-optic Mach-Zehnder interferometer. A method for continuous source polarization modulation was used to measure the Jones matrices [14]. This method of PS-OCT enables full Jones matrix measurement by a single sweep through the wavelength range. The schematic diagram of the system is shown in Fig. 1. Single-mode fiber (Corning HI1060) was used in the fiber-optic components of this system. The light source was a frequency-swept laser (HSL-1000, Santec, Japan) with a center wavelength of 1.06 μm , a wavelength range of 64 nm, full width at half maximum (FWHM) of 61 nm, a wavelength scanning rate of 28 kHz, a duty cycle of 60%, and an average output power of 3.4 mW. The light is directed to an electro-optic polarization modulator (EOM) based on a y-cut, z-propagation, LiNbO₃ waveguide (PC-B4-00-SFAP-SFA-106-UL, EOSpace, US). A linear polarizer (LP) was placed on the input port of the waveguide with its transmission axis aligned 90° to the waveguide (TM mode). Voltage was applied such that the EOM functioned as a variable linear retarder at 45° orientation. The driving waveform was a sinusoidal wave with an amplitude of 2.405 rad and a frequency of 40 MHz. Since the EOM used in this system requires a low voltage as compared to that required by a bulk-crystal-based EOM, a nonresonant driver was sufficient to generate high-frequency modulation. The modulated beam is directed to a 20:80 coupler and split into two beams: one directed to the reference arm and the other to the sample arm. In the sample arm, the beam passes through an circulator (OCST-110112333, Agiltron Inc., US) and a 1:99 coupler. 1% of the beam illuminates a cover slip and a static mirror to generate a phase calibration signal that cancels the phase fluctuations in the system [14, 39]. The cover slip and mirror generate the calibration signals far from the zero-delay position for fine-phase calibration and near the zero-delay position for rough calibration that is for the calibration of a fluctuating spectral shift greater than one sampling time, respectively. 99% of the beam from the 1:99 coupler illuminates the eye after passing through a collimator (F280APC-C, Thorlabs Inc., US), a two-axis galvanometer scanner, an objective lens ($f = 50$ mm), and a Volk 40D ophthalmic lens. The beam diameter incident on the cornea is 1.6 mm. The probing power on the cornea is 537 μW , which is below the maximum power of 1.9 mW to the eye indicated by the ANSI safety standard [40]. The backscattered light from the retina is coupled to the fiber again and directed to a PS detection arm. In the reference arm, the beam is reflected by a retroreflector. The retroreflector and the calibration mirror in the sample arm are mounted together on a single translation stage to maintain the relative depth position constant. The reference beam is directed to the PS detection arm. A LP located on the PS detection arm aligns the state of polarization of the reference beam to 45°. The reference and sample beams are combined at a beamsplitter (BS). The resultant horizontally and vertically polarized components of the beam are split by two polarizing beamsplitters (PBS) and detected at two balanced photoreceivers (1817-FC, New Focus Inc., US). The electric signals are bandpass-filtered from 300 kHz to 40 MHz, and amplified. The signal suppression ratio of this bandpass filter at 60 MHz is higher than -30 dB. In this PS-OCT method, the first-order modulated positive signal and the higher-order signals generated by the polarization modulation cause aliasing and overlap on the nonmodulated signal and the first-order modulated conjugate signal, as shown in Fig. 2. The high suppression ratio of the band-pass filter is crucial to eliminate this aliasing. The signals are acquired by a high-speed two-channel digitizer at 100 MS/s and 12-bit resolution (PCIe-5122, National Instruments, US). The data are buffered in the on-board memory of the digitizer and streamed to the main memory on the motherboard through a high-throughput bus bridge (PXIe-PCIe8371, National Instruments, US) in real time. After acquisition, the data from the main memory are transferred to a hard disk.

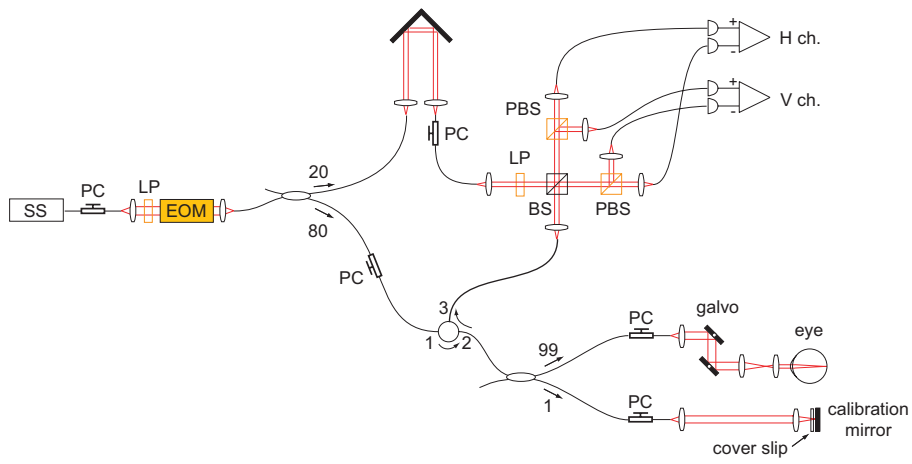


Fig. 1. Schematic diagram of PS-SS-OCT system; SS: frequency-swept laser source, PC: polarization controller, LP: linear polarizer, EOM: electro-optic modulator, BS: beamsplitter, PBS: polarizing beamsplitter, and H ch. and V ch.: balanced photoreceivers for horizontally and vertically polarized signals, respectively.

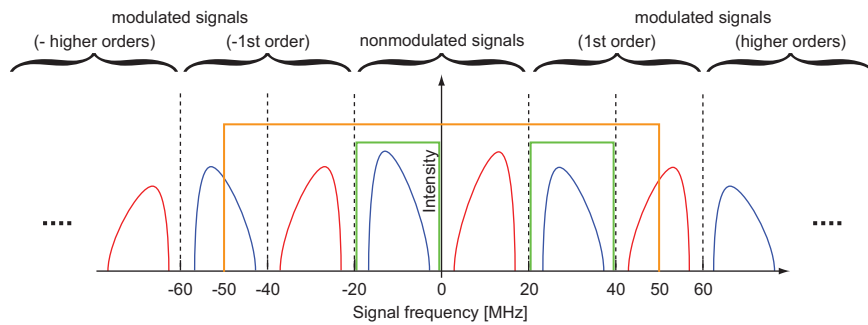


Fig. 2. Diagram of the signal frequency. Red and blue lines show the positive and conjugate signals, respectively. Orange and green windows show the measurable frequency range below the Nyquist frequency (50 MHz) and the extracted region in the demodulation process, respectively.

2.2. Post-processing

The detailed theory and the processing procedure of the method using continuous source polarization modulation have already been described in our previous paper [14]. In short, this method can be explained as follows. The EOM shifts a portion of the signal to the frequency of the modulation, as shown in Fig. 2. The modulated and nonmodulated signals are numerically demultiplexed. From the two photoreceivers in the PS detection arm, four complex OCT signals are obtained by a single depth scan. The depth-resolved Jones matrices are algebraically calculated from these signals [14],

$$\mathbf{J}_{\text{measured}} = \begin{pmatrix} -\left(\tilde{I}_{h0}^* + \frac{\tilde{I}_{h1}^*}{J_1(A_0)}\right) & \tilde{I}_{h0}^* - \frac{\tilde{I}_{h1}^*}{J_1(A_0)} \\ -\left(\tilde{I}_{v0}^* + \frac{\tilde{I}_{v1}^*}{J_1(A_0)}\right) & \tilde{I}_{v0}^* - \frac{\tilde{I}_{v1}^*}{J_1(A_0)} \end{pmatrix}, \quad (1)$$

where \tilde{I}_{h0}^* , \tilde{I}_{h1}^* , \tilde{I}_{v0}^* , \tilde{I}_{v1}^* shows the complex conjugate of the horizontally polarized nonmodulated, first-order, vertically polarized nonmodulated, first-order OCT signals, respectively, and $J_1(A_0)$ shows the zeroth-order Bessel function of the first kind for the amplitude $A_0 = 2.405$ radians.

In order to cancel the birefringence of the fiber-optic components and that of the cornea in the optical path before the retina is illuminated, the Jones matrices on the surface of the retina are averaged for each B-scan and used as a reference matrix to calculate the phase retardation in the sample. Prior to the averaging, global phases of the measured Jones matrices of the retinal surface are normalized by the phases of their first row and first column elements. The measured Jones matrix $\mathbf{J}_{\text{measured}}$ is transformed using the Jones matrix of the retinal surface $\mathbf{J}_{\text{surface}}$, converting the $\mathbf{J}_{\text{measured}}$ into unitary transform of the corresponding Jones matrix of the sample as [41]

$$\mathbf{J}_{\text{measured}}\mathbf{J}_{\text{surface}}^{-1} = \mathbf{J}_{\text{U}} \begin{pmatrix} p_1(i\eta/2) & 0 \\ 0 & p_2(-i\eta/2) \end{pmatrix} \mathbf{J}_{\text{U}}^{-1}, \quad (2)$$

where \mathbf{J}_{U} , p_1 , p_2 , and η are a general unitary matrix, two transmittances of the eigenvectors of the sample, and the phase retardation of the sample, respectively. By carrying out the matrix diagonalization of Eq. (2), we can determine the diattenuation, phase retardation, and the relative orientation of the sample. Polarization-insensitive OCT intensity is determined as the summation of horizontally and vertically detected nonmodulated OCT intensities, namely, $10\log(|\tilde{I}_{h0}|^2 + |\tilde{I}_{v0}|^2)$.

2.3. Calibration methods

The circulator in the sample arm can effectively conserve the optical power in the interferometer; further, its use is necessary in our system, which has a low output power of the light source and a power loss of -4 dB at the EOM. However, a drawback of the use of the circulator at $1.06 \mu\text{m}$ was the occurrence of the undesired polarization mode dispersion (PMD). Although the circulator exhibits only a negligible amount of PMD along the path from port 2 to port 3, i.e., backward path, it exhibits a strong PMD along the path from port 1 to port 2, i.e., forward path. This PMD degrades the point spread function (PSF) of the OCT signal and results in an artifact in the birefringence measurement. If the incident state of polarization is as static as that in a standard non-PS-OCT, the degradation of the PSF can be avoided by aligning the incident state of polarization such that the light passes only through one axis of the birefringent crystal in the circulator. However, since our PS-SS-OCT modulates the incident state of polarization, PMD is unavoidable. In order to solve this problem, the axes of the EOM and the circulator are coincided using a polarization controller (PC) attached to the optical fiber between the EOM and circulator. In practice, calibration is performed to optimize the shape of the PSF of the OCT. In this configuration, modulated beam and nonmodulated beam have different

optical path lengths. Since the difference in path lengths induced by the PMD is static, it can be numerically compensated by applying first-order dispersion (a phase term that is linear in k) to the demultiplexed spectra.

The imperfect alignment of the PC in the reference arm induces an undesired intensity modulation of the reference beam and results in the degradation of the axial resolution. This degradation is because a portion of the nonmodulated OCT signal interacts with the reference modulation and is shifted to the modulated OCT signal and vice versa. In order to align the PC, the sample beam is blocked and the detected signal at the modulation frequency is monitored and minimized. Although the common-path modulation is diminished by the balanced detection, the residual modulation is sufficient for this alignment.

3. *In vivo* imaging of posterior part of human eye

A healthy 27-year-old male volunteer was employed for the polarization-sensitive retinal imaging. An informed consent was obtained from the subject. All protocols adhered to the tenets of the Declaration of Helsinki and were approved by the Institutional Review Board of the University of Tsukuba.

The subject's right eye, which showed no marked retinal disorder, was scanned between fovea and ONH. The lateral range of $5.4 \times 5.4 \text{ mm}^2$, as indicated in the fundus photograph in Fig. 3 (a), was scanned with 512 A-scans \times 200 B-scans in 4.3 seconds. Figures 3 (b)-(g) show the retinal images obtained by the PS-SS-OCT; the single-channel (horizontally polarized nonmodulated) intensity images are shown in (b) and (c), polarization-insensitive intensity images are shown in (d) and (e), and phase retardation images are shown in (f) and (g). In the polarization-insensitive intensity image (Fig. 3 (d)), several blood vessels were observed in the sclera. In the phase retardation image (Fig. 3 (f)), where the phase retardation was depicted based on the color map, and the low-intensity region was masked by black, banding of phase retardation due to birefringence of sclera was observed. Despite the deep penetration, the polarization scrambling at RPE that has been reported previously [8, 12, 17, 18] could not be distinguished from the noise. We expect that it will be improved in the near future by increasing the output power of the light source. In the other B-scan image, shown in Fig. 3 (e), the short posterior ciliary artery [42] was visible. The corresponding phase retardation image in Fig. 3 (g) showed birefringence of the sclera beneath the artery. These images demonstrate the deep penetration of the PS-SS-OCT at $1 \mu\text{m}$.

The single-channel intensity image has a similar image property to a conventional OCT. Both of them are influenced by the birefringence of samples unless the polarization-diverse detection is applied [43]. In Figs. 3 (b) and (c), artificial structures, indicated by green arrows, were observed in the sclera because of their birefringence. Previous studies of $1 \mu\text{m}$ OCT have reported a similar appearance of the banding structure in the sclera (Fig. 8 of Ref. [34] and Fig. 1 (L) of Ref. [32]). Our PS-SS-OCT results confirmed that this structure is attributed to the birefringence of sclera, and it is difficult to distinguish it from real blood vessels in the conventional OCT. Since the polarization-insensitive intensity image has no such artifact, it is essential to clearly observe the blood vessels in the sclera.

Figure 4 shows the images of the ONH. The subject's left eye, which did not show a marked retinal disorder, was scanned. The lateral range of $2.7 \times 2.7 \text{ mm}^2$ was scanned with 512 A-scans \times 200 B-scans in 4.3 seconds. The representative B-scan images of the polarization-insensitive intensity (left) and phase retardation (center) near the center of ONH are shown. In the region between the two green arrows shown in the phase-retardation image, phase retardation was increased as a result of the birefringence of the lamina cribrosa. The sclera and the scleral canal rim on the temporal side, indicated by a white arrow, showed a strong change of the phase retardation. Since the RNFL at temporal and nasal regions is thin and has weak birefringence

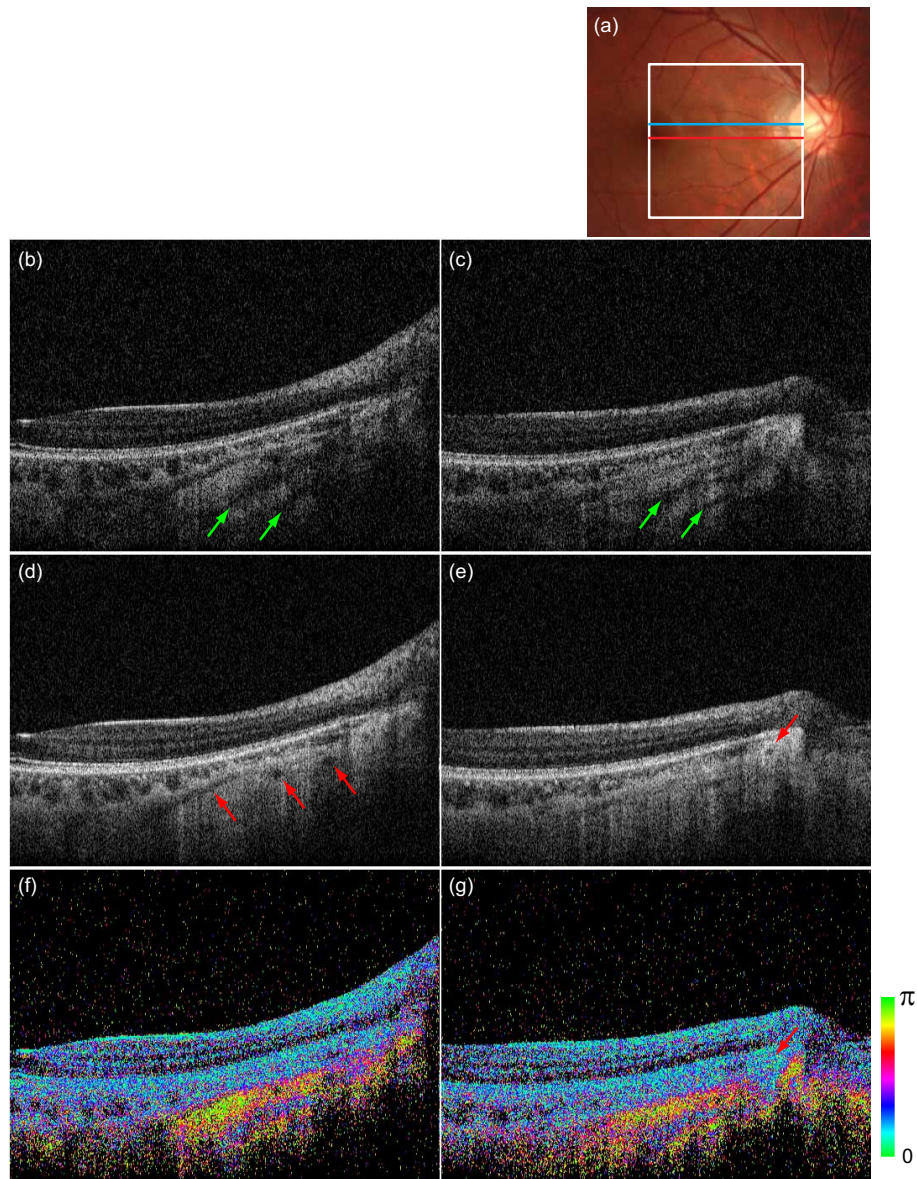


Fig. 3. Retinal images of healthy eye between fovea and ONH indicated in the white box on the fundus photograph (a). The subject's eye was scanned by PS-SS-OCT; scanning range was $5.4 \text{ mm} \times 5.4 \text{ mm}$. (b) and (c): B-scans of single-channel intensity images, (d) and (e): polarization-insensitive intensity images, and (f) and (g): phase-retardation images. The red and blue lines on (a) represent the scanning positions of (b), (d), and (f) and (c), (e), and (g), respectively. The image size of the B-scans is $5.4 \text{ mm} (x) \times 1.96 \text{ mm} (z)$. The artificial structures due to birefringence of the sclera are indicated by green arrows in (b) and (c). The blood vessels in the sclera and short ciliary artery are indicated by red arrows in (d), (e), and (g), respectively. A movie of the polarization-insensitive intensity and phase-retardation images scanned from inferior to superior regions and its high-quality version are available ([Media 1](#) and [Media 2](#)).

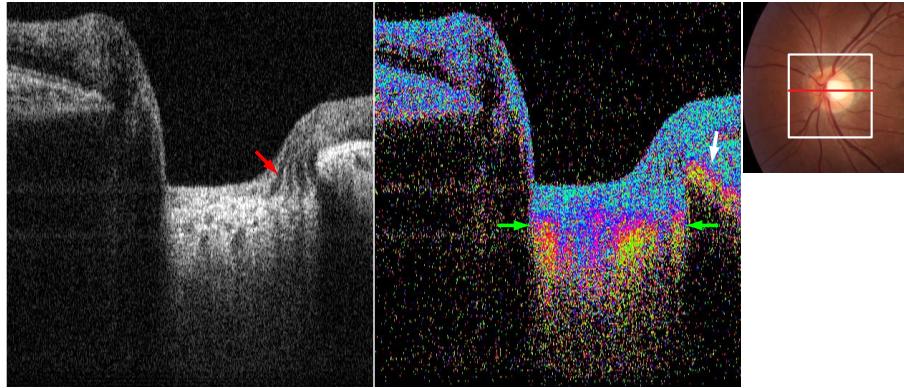


Fig. 4. Polarization-insensitive intensity (left) and phase retardation (center) images of ONH. The image size is 2.7 mm (x) \times 1.89 mm (z). The red line in the fundus photograph (right) shows the position of the B-scan. The white box indicates the scanned region to obtain the volumetric data shown in Fig. 5.

[5–7, 11, 44], the change of the phase retardation of the RNFL in the left and right sides of Fig. 4 was not clearly visible. A characteristic structure called nerve fascicles [45] present at the bent nerve fiber indicated by the red arrow and the connection of the structure to lamina cribrosa were visible in the intensity image. The nerve fascicles did not show birefringence because they were parallel to the probing beam.

Figure 5 shows the *en face* slices of the intensity and phase retardation volumes that are shown in Fig. 4. On the prelaminar region at 52 μm from the bottom of the ONH, shown in Figs. 5 (a) and (d), phase retardation in the ONH did not show significant variation. Figures 5 (b) and (e) show the region of lamina cribrosa at a depth of 170 μm from bottom of the ONH. Individual pores of the lamina cribrosa were observed in the intensity image (b). The phase retardation image (e) showed inhomogeneous birefringence of the lamina cribrosa. In the case of this subject, the phase retardation was high on the nasal and temporal sides. Also in the retrolaminar region at a depth of 319 μm shown in Figs. 5 (c) and (f), the phase retardation was inhomogeneous. The inferior half of the lamina cribrosa showed high phase retardation. This pattern of phase retardation was not clearly observed in the corresponding intensity image (c). This result might imply that the lamina cribrosa has different characteristics at different regions of the ONH; however, further study is required to confirm it.

4. Discussions

4.1. Sensitivity and axial resolution

Optimization of the system sensitivity was important to improve the image quality under the conditions of limited optical power of the light source and power loss at the EOM. In order to improve the system sensitivity, we optimized the balanced detection and the power efficiency of the interferometer.

Using balanced detection, we can minimize relative intensity noise of the frequency-swept laser. However, in practice, the wavelength dependence of a beamsplitter or a fiber coupler in the detection arm degrades the common mode rejection ratio [46]. For PS detection, polarization-maintaining fiber-optic components can be employed [14]. At a wavelength of 1 μm , however, the wavelength dependence was considerably high; the deviation in the splitting ratio exceeded $\pm 50\%$ at the edges of the spectrum. In order to reduce the wavelength dependence, we employed the bulk-optical PS detection arm, as described in Section 2. By using this PS detection

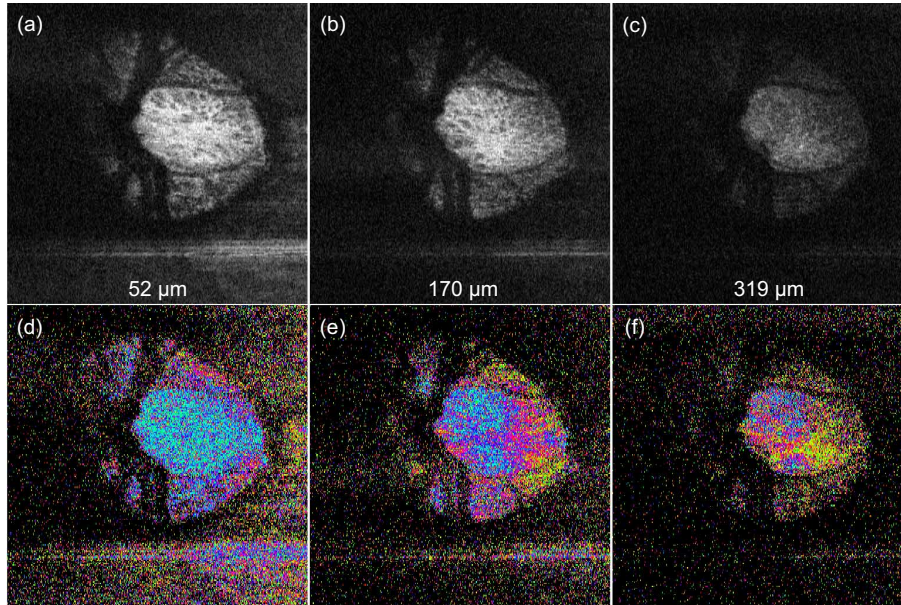


Fig. 5. Images of *en face* intensity (upper) and phase retardation (lower) volumes of ONH. The image size is $2.7 \text{ mm} \times 2.7 \text{ mm}$. The volumes are sliced at depth positions of $52 \mu\text{m}$ (left), $170 \mu\text{m}$ (center), and $319 \mu\text{m}$ (right) from the bottom of the ONH. A movie of the *en face* slices of the volumetric data from anterior to posterior regions and its high-quality version are available ([Media 3](#) and [Media 4](#)).

arm, the deviation in the splitting ratio was reduced to less than $\pm 3\%$ over the spectral range. Owing to this bulk detection arm, 4 dB improvement of the system sensitivity was confirmed.

An optical circulator can be used to increase the power efficiency of the interferometer, and it has been widely used at $1.3 \mu\text{m}$ wavelength [47]. However, its use in OCT systems at $1 \mu\text{m}$ wavelength was not common [27–33, 35, 36]. We used the circulator at $1 \mu\text{m}$ wavelength and developed a method to calibrate the PMD to prevent its negative effect, as described in Sec. 2.3. In theory, a circulator can improve the sensitivity by a gain of 6 dB with respect to that of a system with a 50:50 coupler in the sample arm. The gain in the sensitivity of our system was measured to be 5 dB; the deviation from the theoretical value given above is attributed to the insertion loss of the circulator.

After the above-mentioned optimization and improvements, the resultant system sensitivity was measured to be 94.2 dB near the zero depth and decreased at a rate of -8.1 dB/mm in the measurement range of 2.67 mm in tissue. The total coupling loss in the sample arm and the PS detection arm was measured to be -4.2 dB . By taking the coupling loss into consideration, the shot-noise-limited sensitivity [38] was calculated to be 99.4 dB. The difference of 5.2 dB between the theoretical and experimental values can be attributed to imperfect balanced detection, because the BS in the PS detection arm still showed slight wavelength dependence.

By performing the calibration of the PC between the circulator and the EOM, the axial resolution was also optimized together with the sensitivity; the axial resolution was measured to be $11.0 \mu\text{m}$ in tissue under the assumption that the refractive index is 1.38. The theoretical axial resolution is expected to be $5.9 \mu\text{m}$ in tissue using the parameters described in Sec. 2. The discrepancy between the theoretical and experimental values is explained by the reduced effective FWHM in the experiment, because a gaussian window was applied to reshape the spectrum. The side peak observed in the polarization-insensitive intensity because of PMD was less than

the main peak by -20 dB. The above results show that we could effectively improve the system performance without facing significant drawbacks.

4.2. *The advantage of Jones formalism compared to Stokes-Mueller formalism for analyzing PS-OCT*

To utilize the circulator with PMD, two orthogonal incident states of polarizations have to be aligned to the axes of the circulator as described in section 2.3. In our system, it was implemented by using the method of continuous source polarization modulation. PS-OCT with continuous source polarization modulation was originally developed by Jiao et al. using the time domain OCT detection scheme [48]; subsequently, it was developed by Yamanari et al. using the Fourier domain detection scheme [14, 49]. This continuous source polarization modulation can be regarded as multiplexing two orthogonal source polarization states in the signal frequency. This approach for polarization modulation forms the basis of our strategy to overcome PMD. However, previous studies suggested that the incident states of polarization should be orthogonal on the Poincaré sphere, e.g., horizontal and circular polarizations, and not orthogonal as the basis of Jones vector [41, 50, 51].

These contradictory arguments arise from the difference between the Stokes-Mueller formalism and Jones formalism. Stokes vectors cannot represent the phase relationship between the two beams because the dimension of Stokes vector is intensity, and in Stokes vectors, coherence among the vectors does not exist. On the Poincaré sphere, relative phase between two states of polarization cannot be described. The change of the Stokes vectors is tracked in the intensity domain without using the relative phase between the polarized beams. In contrast, Jones vectors can represent the relationship between two states of polarization from their absolute phases, because these phases are treated as coherent in the Jones formalism. This difference made our method using two orthogonal incident states of polarization possible. Our approach has an advantage when we need to utilize the circulator with PMD to optimize the efficiency of the interferometer, as we have shown in Sec. 4.1.

5. Conclusion

In conclusion, we developed a PS-SS-OCT system for imaging at $1 \mu\text{m}$ wavelength. It enabled to visualize the birefringence of the structures of the deep posterior part of the eye, such as sclera and lamina cribrosa, *in vivo*. The sufficiently high system sensitivity for retinal imaging was achieved by using the circulator and the bulk-optical PS balanced detection arm. The problematic PMD of the circulator was overcome by our Jones-matrix approach. The preliminary measurements of *in vivo* sclera and lamina cribrosa showed that the artificial structure observed in the conventional intensity images as a result of birefringence could be clearly distinguished from the real structure by polarization-diverse detection; further, the phase-retardation images showed an enhancement in the contrast of these fibrous tissues, which were not clearly visible in the intensity images. To the best of our knowledge, this is the first demonstration of PS-OCT at $1 \mu\text{m}$ for retinal imaging. Our PS-SS-OCT at $1 \mu\text{m}$ would have a potential to reveal retinal diseases accompanied by birefringence changes in deep posterior part of the eye.

Acknowledgement

This research was supported in part by Japan Science and Technology Agency.